

Direct visualization of visible-light hyperbolic plasmon polaritons in real space and time

Atreye Ghosh,^{1,*} Calvin Raab,^{1,2,*} Joseph L. Spellberg,^{1,2} Aishani Mohan,^{1,2} and Sarah B. King^{1,2,†}

¹James Franck Institute, The University of Chicago, Chicago, IL 60637, USA

²Department of Chemistry, The University of Chicago, Chicago, IL 60637, USA

(Dated: June 17, 2025)

Hyperbolic materials support exotic polaritons with hyperbolic dispersion that enable subdiffraction focusing and enhanced light-matter interactions. Visible-frequency hyperbolic plasmon polaritons (HPPs) offer significant advantages over hyperbolic phonon polaritons, which operate in the infrared frequency range — namely lower losses and greater technological relevance. However, these HPPs remained experimentally inaccessible until the recent identification of molybdenum(IV) oxychloride (MoOCl₂). Here we achieve the first direct real-space and real-time visualization of hyperbolic plasmon polaritons in natural materials using time-resolved photoemission electron microscopy with femtosecond time resolution and nanometer spatial resolution. Our direct imaging enables measurement of HPP propagation velocities and lengths, real-time observation of plasmon-material edge interactions, experimental validation of hyperbolic dispersion through polarization-dependent experiments, and direct visualization of hyperbolic focusing phenomena. This spatiotemporal visualization validates theoretical predictions while establishing an experimental foundation for exploiting these unusual light-matter states in fundamental studies of hyperbolic media and nanophotonics.

Imagine materials that can focus light to dimensions smaller than its wavelength, amplify photon emission by orders of magnitude, and manipulate light in ways that seem to defy conventional optics [1–3]. These extraordinary optical capabilities arise from polaritons in hyperbolic materials — materials where the frequency-dependent permittivity tensor elements have opposite signs along orthogonal axes. Polaritons are hybrid states of light and matter, and in hyperbolic materials, polariton wavevectors \mathbf{k} have hyperbolic isofrequency contours instead of the circles and ellipses found in conventional materials (Figure 1A) [4]. First predicted by Veselago in 1968 [5], hyperbolic materials remained largely theoretical curiosities until researchers developed artificial metamaterials to validate the decades-old predictions [6, 7]. However metamaterials only act as effective hyperbolic materials at large length scales; natural materials where hyperbolicity is maintained down to nm scales have been very limited [8, 9].

Hyperbolic light-matter states, polaritons, can occur with different matter excitations and in general exhibit direction-dependent excitation and dispersion and hyperbolic focusing. Hyperbolic phonon polaritons, light-matter states of *phonons* in the terahertz and infrared portion of the electromagnetic spectrum, have been observed in natural materials such as hexagonal boron nitride [10], calcite [11], alpha-phase vanadium dioxide [12], and alpha-phase molybdenum trioxide [13]. Hyperbolic plasmon polaritons (HPPs), on the other hand, are light-matter states of *electrons*. Plasmon polaritons typically have fewer losses than phonon polaritons and can operate in the visible spectrum, where most optical technologies have been developed. Naturally occurring hyperbolic materials capable of supporting visible-frequency HPPs proved elusive until 2020 when theory revealed that

molybdenum(IV) oxychloride (MoOCl₂, Figure 1B) [14] possesses the required combination of metallic behavior along one crystal direction and insulating behavior along the others [15, 16]. Recent experiments in MoOCl₂ revealed long propagation lengths, signatures of electron correlation [17], and hyperbolic lensing of plasmons launched from gold emitters [18], all tantalizing properties of HPPs. However, no experiment has directly visualized how these collective light-electron modes actually move and evolve in space and time — until now.

In this work, we provide the first direct visualization of HPP dynamics in MoOCl₂ with sub-optical cycle time resolution (<1 fs) using time-resolved photoemission electron microscopy (TR-PEEM). We directly observe the propagation of HPPs, determine the phase and group velocities, and observe HPP reflection from crystal edges — all with nanoscale spatial resolution. These measurements finally enable experimental validation of theoretical predictions made sixty years ago and open the door for the prediction and testing of new theories in hyperbolic materials.

MoOCl₂ is a biaxial van der Waals (vdW) material with properties of a quasi one-dimensional metal with both in- and out-of-plane anisotropy in the dielectric tensor [15, 19]. Calculations predict the primary hyperbolic region occurs from the infrared to around 430 nm, where $\epsilon'_x(\omega) < 0$ and $\epsilon'_y(\omega) > 0$, giving rise to in-plane hyperbolicity [18, 19]. This anisotropy originates from the Mo–O bonds along the crystalline *a*-axis and the Mo–Cl bonds along the *b*-axis, Figure 1B [16, 19]. Along the *b*-axis, an orbital selective Peierls phase results in Mo–Mo dimers and flat d_{xy} bands, while the *a*-axis shows metallic character with highly dispersive d_{yz} and d_{xz} bands [19]. The flat bands along the *b*-axis also result in electron-electron correlation effects, as seen in low-temperature resistance measurements [20]. The *b*-axis shows strong interband transition influence resulting in higher losses, with a large peak in $\epsilon''_y(\omega)$ at 2.9 eV. In contrast the *a*-axis has very low losses since most transitions are symmetry forbidden [16]. Thus, the *a*-axis is ideal

* These two authors contributed equally.

† sbking@uchicago.edu

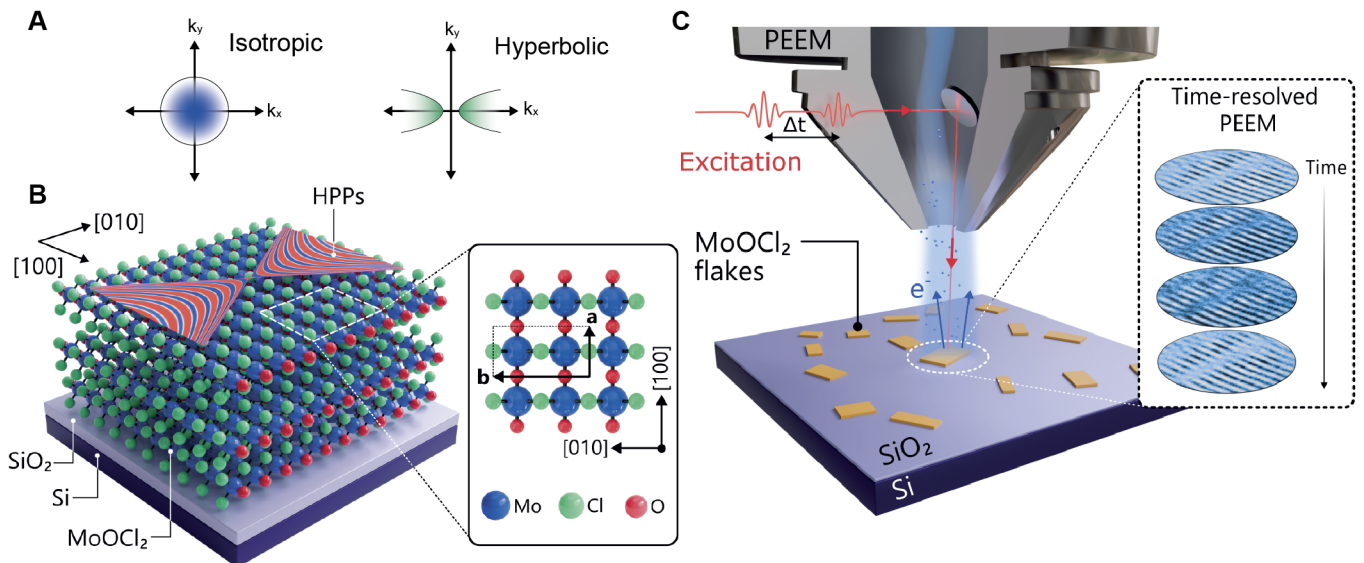


FIG. 1. **A** Isofrequency surfaces for an isotropic material where $\varepsilon'(\omega)$ has the same sign in the x and y directions versus a hyperbolic iso-frequency surface where $\varepsilon'_x(\omega)$ is negative while $\varepsilon'_y(\omega)$ is positive. **B** A schematic of the MoOCl_2 samples used in these experiments with the inset showing the difference in Molybdenum bonding in the a and b crystal directions that gives rise to hyperbolic plasmons. **C** The TR-PEEM spectrometer with the delay between two interferometrically locked ultrafast laser pulses, Δt , enables direct imaging of the evolution of the hyperbolic plasmons in space with sub-cycle time-resolution.

for low-loss plasmonic propagation in the visible region.

Time-resolved photoemission electron microscopy (TR-PEEM) is a wide-field electron microscopy technique that leverages the high spatial resolution of electron microscopy with the time, polarization, and energy control of photon probing. As depicted in Figure 1C, PEEM for plasmonic imaging uses an ultrafast pulsed laser to generate plasmonic excitations and photoemit electrons, forming a wide field microscope image of plasmonic fields [21]. Edges, grooves, or defects in the material generate the momentum to launch a plasmon polariton without prism or nanoscale tip coupling. PEEM can image plasmonic field distributions with and without time-resolution. With static PEEM, the superposition between the optical probe and the excited plasmonic wavepacket from two or more photons within the same ultrafast laser pulse results in interference fringes due to multiphoton emission [22–24]. TR-PEEM excites and probes the sample with two interferometrically locked laser pulses with a time-delay, Δt , that is controlled with a precision delay stage. Scanning the delay between two pulses enables wide-field time-resolved imaging to elucidate plasmon dynamics with sub-cycle temporal resolution, Figure 1C. Unlike other approaches to investigate the dynamics of plasmons in 2D materials [25], PEEM is a wide-field imaging technique rather than a tip-enhanced technique that requires raster scanning across a sample. PEEM makes high time-resolution experiments much easier and maintains relative phase information over the entire image as all points in space are imaged simultaneously. Predominantly used to image plasmon propagation on Au and Ag surfaces in space and time [21, 26–28], PEEM has been more recently used to probe polaritons in 2D layered materials such as plasmon

polaritons in MXenes [29] and exciton polaritons in MoS_2 [30].

PEEM IMAGING OF HPPS

In this study, we validate that PEEM can image HPPs in MoOCl_2 by measuring three HPP hallmarks: directional plasmon propagation along the a axis of MoOCl_2 , dispersion of the HPP to the right of the light line, and hyperbolic focusing. PEEM at near-normal incidence has excellent control of light polarization in plane [31–34] enabling us to directly determine how changing the in-plane laser polarization modifies the directional plasmon propagation in MoOCl_2 . Figure 2A and B show two polarization-dependent PEEM (PD-PEEM) images of a 2D MoOCl_2 flake excited with light polarized along the a axis of the crystal or along the b axis of the crystal. Interference fringes are only present along the a axis; they require light polarized perpendicular to the a axis, exciting transverse magnetic plasmons, a signature of HPPs. In contrast, isotropic plasmon polaritons can be excited in arbitrary directions determined by the polarization of the incident field and the geometry of the edge that generates the momentum required for launching plasmon polaritons [29]. Notably, to complement the PD-PEEM measurements, we also conducted polarization-resolved Raman spectroscopy on the same flakes, which revealed strong anisotropy in the Raman response as a function of the relative orientation between the crystallographic axes of MoOCl_2 flake and the laser polarization (Figure S11).

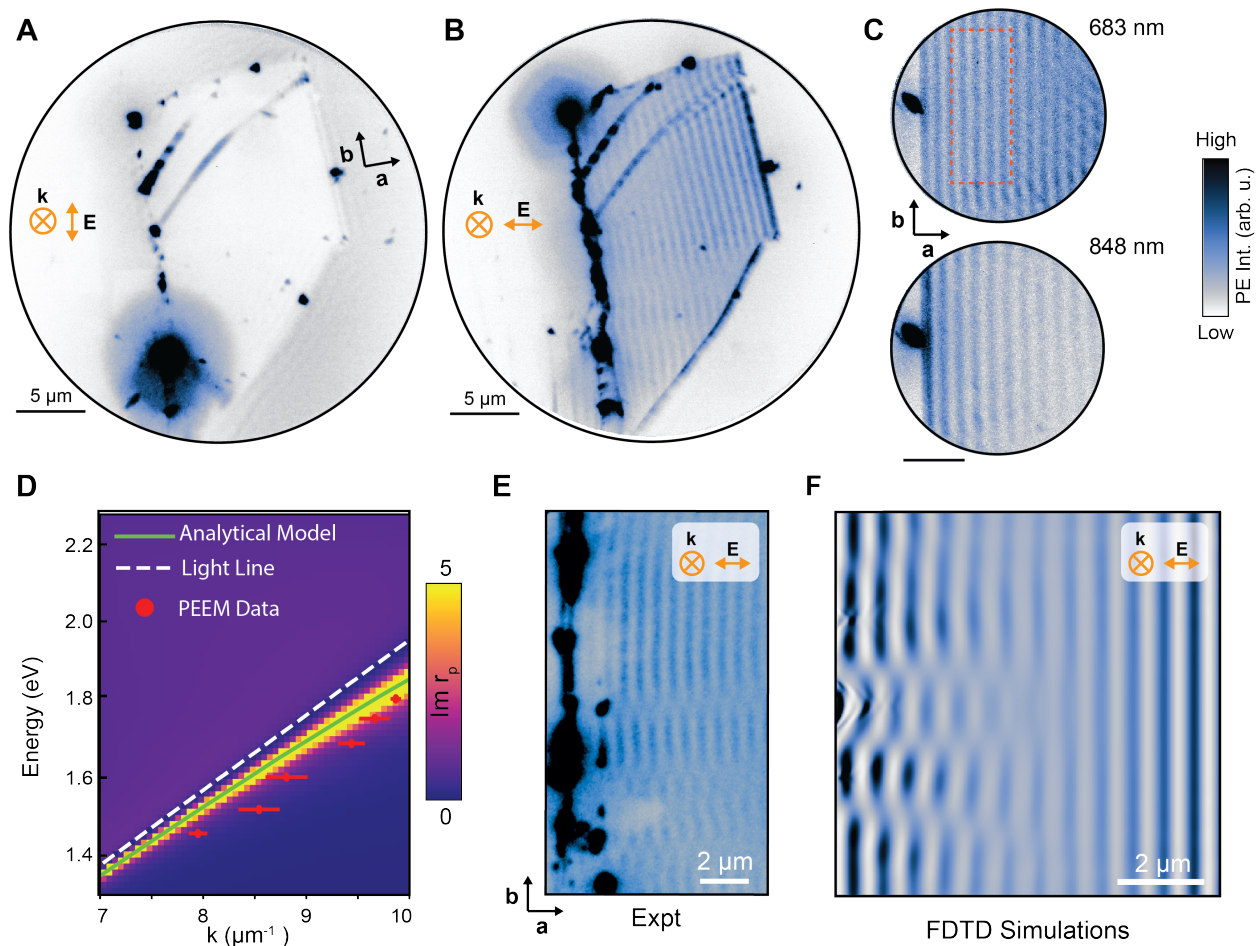


FIG. 2. **A** and **B** Polarization-dependent PEEM of MoOCl_2 at near-normal incidence with laser illumination of wavelength 787 nm. HPPs are clearly observed only when the laser polarization is aligned with the **a** axis and where the necessary momentum for coupling to the HPP is provided by the edge discontinuity of the MoOCl_2 flake. **C** HPP fringe spacing changes with incident light wavelength (energy). **D** Comparison of the HPP dispersion to analytical and numerical models show fairly good agreement. **E** Natural curves in an as-exfoliated MoOCl_2 flake at wavelength 774 nm cause hyperbolic lensing consistent with a PEEM image generated with FDTD simulations on under identical conditions, **F**.

Repeating static PEEM experiments as a function of photon energy, we observe that the fringe spacing changes with energy (Figure 2C), based on which we extract the dispersion of the plasmon polariton (Figure 2D) (also see Figure S13). The experimental data points are in good agreement with analytical calculations of the dispersion along the *a* axis from reported dielectric functions in reference Zhao *et al.* [15]. Consistent with previous reports, we find that the theoretically predicted dispersion exhibits slightly smaller k_x compared to experimental data [17]. This has been attributed to electron correlation effects not fully captured within the dielectric function calculated by DFT [15, 17]. Notably our experiments also suggest that the hyperbolic region is narrower than predicted from current theoretical models. We do not see evidence of HPPs in experiments at 2.4 eV (516 nm) and higher energies (Figure S14) as predicted by Zhao *et al.* [15]. Higher level theoretical methods and experimental methods that can capture the momentum

resolved dielectric function, are likely called for to accurately predict the dielectric function at higher energies [17, 35–37].

The last hallmark of HPPs is hyperbolic focusing. As formulated in the Huygens-Fresnel principle, an optical wavefront can be reconstructed from dipole emitters, each with a phase-front shape corresponding to the reciprocal space isofrequency surface. For hyperbolic materials, this results in geometric optics not seen in isotropic materials; for instance, a curved flake edge will result in plasmonic focusing in MoOCl_2 [17]. Such hyperbolic focusing is readily apparent in Figure 2E where natural curvature in the flake edge that launches the plasmons causes a focusing of the plasmonic fringes in agreement with finite difference time domain (FDTD) simulations, Figure 2F. In contrast, in isotropic materials such as Ag, the same edge geometry causes the fringes to diverge and host spherical wavefronts (see Supplementary Information and Figure S2).

In our experimental data, we rule out so-called “ghost”

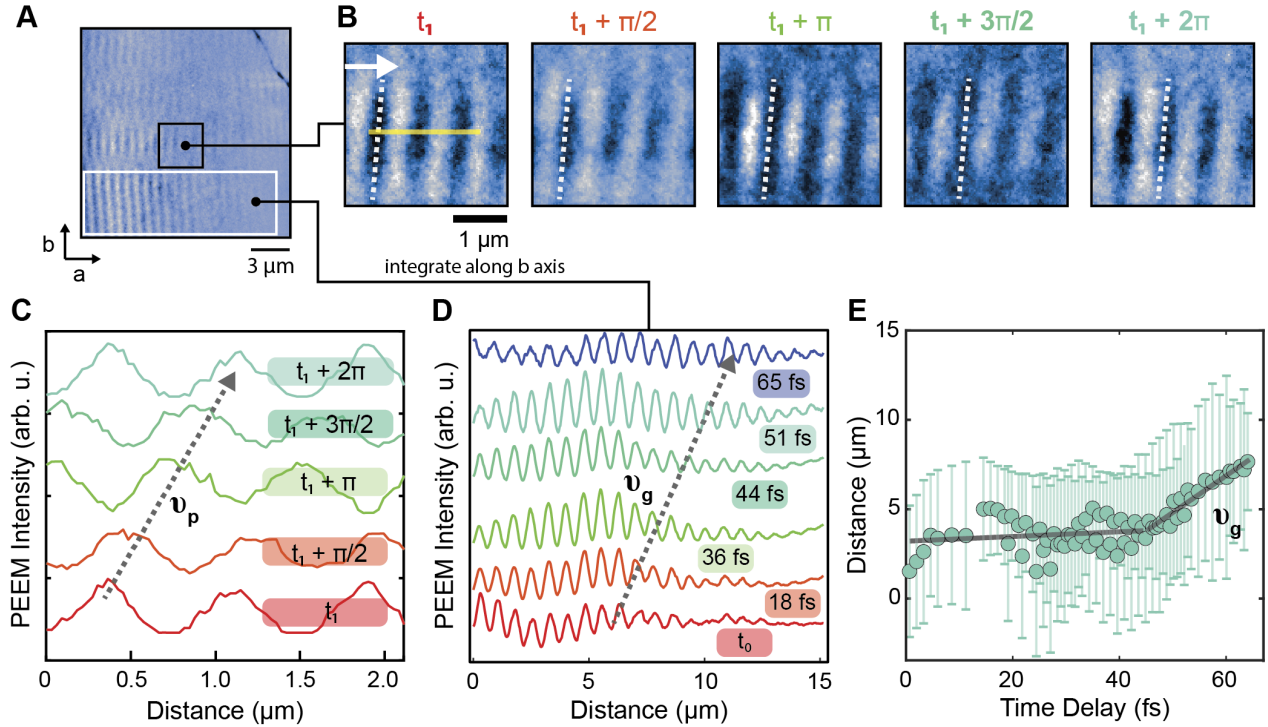


FIG. 3. **A** Image at $\Delta t = 0$ for an interferometric PEEM experiment with $h\nu = 1.6$ eV. **B** Expansion of the black box from **A** for different phase delays of the two phase-locked laser pulses. For this photon energy a phase shift of $\pi/2 = 0.645$ fs. The same peak is traced in a white dotted line through each image. **C** Linecuts along the yellow line in **B** for each phase delay. **D** Linecuts from the white box in **A** where the intensity has been integrated along the b axis showing the group velocity of the HPP wavepacket as it propagates from the edge. **E** The fit gaussian center of the HPP wavepacket as it propagates away from the edge as a function of time. The group velocity is fit to the propagating wave between 44 and 64 fs.

modes [11], characterized by a complex k_z with both evanescent and propagating characters and previously reported in MoOCl_2 [18], based on the surface sensitivity of our imaging method and the long propagation lengths observed. Ghost modes arise at energies where $\min(\varepsilon_x, \varepsilon_y) < \varepsilon_z < \max(\varepsilon_x, \varepsilon_y)$ occur within the bulk and exhibit significant losses [18, 38]. In contrast, PEEM is a highly surface sensitive technique, relying on photoemission for signal detection [39] and the fields we observe propagate over distances exceeding $15 \mu\text{m}$ (discussed later in this paper), inconsistent with short decay length one would expect for lossy ghost modes. Overall, based on the directional plasmon propagation, dispersion, and hyperbolic focusing observed in our static images, and eliminating possible contributions from ghost modes, we conclusively verify the hyperbolic nature of plasmon polaritons in MoOCl_2 .

SPACE-TIME IMAGING OF HPPS

Time-resolved imaging of the dynamics of HPPs in space and time allows for direct extraction of their phase and group velocities and watching the interaction of HPPs with nanoscale structures such as flake edges. Using a Michelson interferometer (Figure S15), we create a pair of phase-

locked laser pulses that are controlled in time with a mechanical stage that can precisely create time-steps < 1 fs, to directly image the dynamics of HPPs. The two laser pulses incident on the sample create a complex set of interferences due to light-light, light-plasmon, and plasmon-plasmon interactions. We apply time-domain Fourier filtering [21, 24, 40], as described in the Supplementary Information (Figure S3), and extract the dynamics that are first order in the driving laser frequency.

These dynamics enable us to extract the phase (v_p) and group (v_g) velocities of HPPs in MoOCl_2 , directly observing the impact of MoOCl_2 's dispersion on the dynamics of HPP propagation. A snapshot of an interferometric TR-PEEM experiment with 1.6 eV photons is shown in Figure 3A. Zooming in on a portion of the flake, Figure 3B, one can directly observe the dynamics of the HPPs within an optical cycle (~ 2.6 fs). The data clearly shows oscillatory behavior as the HPP interacts and interferes with the laser pulse. While the carrier envelope phase (CEP) of the driving laser is not stabilized between different repetitions of the laser, the relative CEP between two pulses within one repetition is constant and has a locked phase relationship. This provides access to directly image the sub-cycle dynamics and extract the phase velocity of the HPP. Line profiles from the yellow line in Figure 3B are shown in Figure 3C. Tracing the spatial

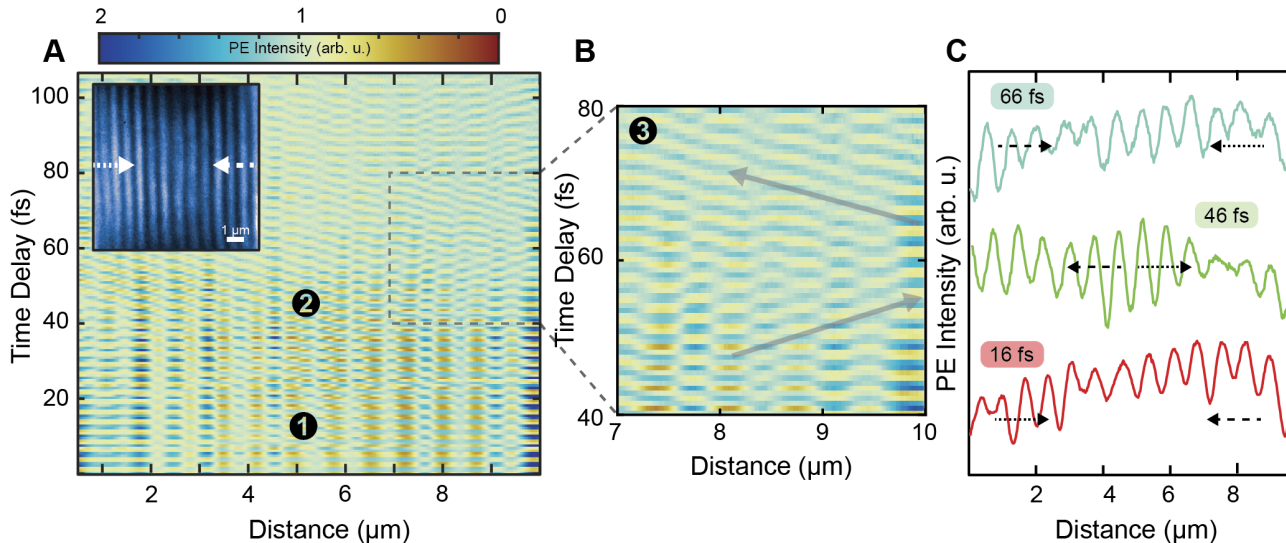


FIG. 4. **A** Space-time contour plot of a PEEM movie (Supplementary Movie Flake B) where HPPs are launched from the edges of the inset flake snapshot along the a axis. As a function of time the HPP wavepackets propagate away from the edges (1), pass each other in the middle of the flake (2), and reflection off of the other edge (3). A zoom in of the reflection dynamics are shown in **B** where the arrows trace the dynamics of the HPP wavepacket. **C** Accompanying line cuts integrated along the b axis where the dotted and dashed arrows demonstrate the direction of the HPPs launched from the left and right edges, respectively as they undergo propagation.

dynamics of a peak in the line profile as a function of time, we extract a plasmon phase velocity of $2.93 \pm 0.02 \times 10^8$ m/s, or $0.98 \pm 0.07 c$, in good agreement with calculations as described in the Supplementary Information.

From the same experiment one can also directly visualize how a plasmon wavepacket moves away from the edge of a MoOCl_2 flake and determine the corresponding group velocity. As shown in Figure 3D, the initial excitation fringe profile moves to the right as a function of time. Fitting these fringe profiles to a Gaussian wavepacket envelope, as described in the Supplementary Information (Figure S6 and S8), we can quantitatively measure how the plasmon wavepacket moves in time, Figure 3E. There are two regions in the dynamics, a quasi-stationary initial period, and then a propagating period. Such quasi-stationary plasmon polaritons have been observed previously in experiments on Au and Ag noble metal surfaces due to the strong influence of the edge launching the plasmons [41]. In the propagating period we extract a plasmon group velocity of $2.0 \pm 0.3 \times 10^8$ m/s, or $0.69 \pm .09 c$. This experimental group velocity is slower than calculations based on an analytical model of the HPP dispersion, where $v_g = \partial\omega(k)/\partial k$ in Figure S5 predicts a plasmon group velocity of $0.88 c$. One possible reason for this discrepancy could be the role of electron correlation in MoOCl_2 . The analytical model used to calculate v_g is based on electronic structure calculations of the dielectric tensor that do not account for electron correlations. As noted in reference [17], accounting for electron correlations pushes the dispersion further to the right of the light line, decreasing the group velocity, consistent with what we observe experimentally in our time-resolved data.

REFLECTION OF HPPS ENABLED BY LONG PROPAGATION

One of the many intriguing aspects of HPPs is the unusual ways they may interact with edges, leading to effects like negative refraction [42] or possible Goos-Hänchen shifts [43–46]. MoOCl_2 HPPs in our experiments have long-enough propagation lengths and lifetimes that we may capture the dynamic interaction of HPPs reflecting off the edges of MoOCl_2 flakes, Figure 4. Two sets of HPPs are launched from parallel edges of a MoOCl_2 flake. These HPP wavepackets propagate toward the flake center, pass each other, and then reflect off of the opposite edge before finally decaying. While the flake geometry of these experiments does not allow for imaging negative refraction or Goos-Hänchen shifts, our experiments demonstrate that MoOCl_2 is a fruitful playground to realize such experiments, even at room temperature.

This experiment also showcases the surprisingly long propagation length of HPPs in MoOCl_2 . Taking our experiments in aggregate, we determine estimates of the propagation lengths for the HPPs from the different data sets, as described in the Supplementary information. Propagation lengths range from 2 to $30 \mu\text{m}$, depending on the type of data (static or time-resolved) used for our calculations. We measure the longest propagation lengths of approximately $30 \mu\text{m}$ in our time-resolved reflection experiments where the propagation length is not pulse width limited. These propagation lengths are longer than had previously been estimated from static sSNOM experiments [16, 17], where they observe propagation lengths of approximately $1.5 \mu\text{m}$.

It is possible that the difference in the excitation and detection of the HPPs impacts the measured propagation lengths and invites further investigation. However, the propagation lengths we observe suggest that not only could MoOCl_2 be an interesting material for testing fundamental questions in physics and nanophotonics, but that it could be used in nanophotonic devices [47].

DISCUSSION

Sixty years after Veselago’s theoretical prediction of materials with hyperbolic dispersion, we have achieved the first direct spatiotemporal visualization of hyperbolic plasmon polaritons in the visible portion of the electromagnetic spectrum in a natural material. This represents a breakthrough in our ability to observe and understand unusual light-matter interactions that have remained hidden from experimental view since their theoretical conception. By combining time-resolved photoemission electron microscopy with sub-optical cycle temporal resolution and nanoscale spatial precision, we have bridged the gap between decades of theoretical predictions and experimental reality.

Our experimental achievements extend far beyond simple observation. We have directly measured the phase and group velocities of visible-frequency HPPs and observed HPP reflection from crystal edges—all phenomena that could previously only be inferred or modeled. The exceptionally long propagation lengths we observe far exceeding previous estimates, reveal that MoOCl_2 supports remarkably low-loss hyperbolic plasmons even at room temperature, challenging existing theoretical frameworks and suggesting that electron correlation effects play a more significant role than previously understood.

These capabilities transform hyperbolic plasmonics from a theoretical field into an experimental science. Researchers can now directly test theoretical predictions about negative refraction, Goos-Hänchen shifts, and other unusual phenomena in hyperbolic media. Our technique opens pathways to investigate fundamental questions about the limits of light confinement, the role of material anisotropy in electromagnetic propagation, and the interplay between electronic correlations and collective excitations in van der Waals materials. The ability to visualize these dynamics in real time will undoubtedly reveal new physics that cannot be predicted from static measurements alone.

Looking forward, this work establishes visible-frequency hyperbolic plasmonics as a platform for next-generation nanophotonic technologies [48, 49]. The combination of subdiffraction focusing, enhanced light-matter interactions, and room-temperature operation positions MoOCl_2 and related materials at the forefront of applications ranging from quantum information processing to ultra-sensitive biosensing. More broadly, our spatiotemporal imaging approach provides a new experimental paradigm for studying collective excitations in anisotropic materials, promising to accelerate discoveries across condensed matter physics, nanophotonics, and quantum optics [50–52]. The exotic world of

hyperbolic materials, long confined to theory, is now open for experimental exploration.

METHODS

A. Sample preparation

Single crystals of MoOCl_2 were purchased from hq graphene. Using mechanical exfoliation with scotch tape and transfer with PDMS viscoelastic stamping, flakes of MoOCl_2 were deposited onto silicon wafers (n-doped Si(100), $\rho = 1 - 10 \Omega$) with native oxide purchased from University Wafer. This process produces separated flakes with lateral sizes of tens of microns (see Figure S12A). All exfoliation was done in a N_2 glove box prior to transfer into ultra-high vacuum (UHV) to maintain high quality samples even though no evidence for atmospheric degradation was observed. Atomic force microscopy was conducted in the tapping mode to determine the thickness of the flakes (see Figure S12C). Raman spectroscopy (Figure S11) was carried out in a HORIBA LabRAM HR Evolution confocal Raman microscope.

B. PEEM experiments

All PEEM experiments were performed under ultra-high vacuum ($< 1 \times 10^{-10}$ mbar) using a photoelectron microscope from Focus GmbH. The microscope has a spatial resolution better than 40 nm. One-photon photoemission microscopy (1P-PEEM) was carried out with a 100 W broadband mercury arc lamp ($h\nu \leq 5.1$ eV) under grazing incidence (65° to the surface normal) to locate the MoOCl_2 flakes on the surface and obtain an overview of the flake geometry (Figure S12B).

Initially unoccupied intermediate states, such as plasmon resonances, may be pumped and probed in nP-PEEM (with $n \geq 2$) so that they may contribute to the PEEM signal. Monochromatic nP-PEEM ($n = 4$) experiments were conducted with fundamental ($1.35 \leq 1h\nu \leq 1.9$ eV, 5 – 30 nJ pulse energy, 30 – 40 fs pulse duration) of a home-built optical parametric amplifier (OPA). The OPA was pumped by the second harmonic ($2h\nu = 2.4$ eV) of a Coherent Monaco with a repetition rate of 4 MHz. The laser spot sizes on the sample were approximately 300 to 1000 μm^2 . For all time resolved results presented in this manuscript with excitation $h\nu = 1.6$ eV, photoemission from MoOCl_2 is a 4PPE process, as shown in Figure S16.

The linearly polarized laser beam was directed to the sample either at near-normal incidence (4° to the surface normal) via a rhodium mirror inside the microscope column (see Fig. 1C). In this configuration, the laser polarization is effectively in the plane of the sample surface. $\lambda/2$ waveplates were used to tune the in-plane laser polarization with respect to the edges of the MoOCl_2 flakes. Details of laser polarization calibration can be found in references Joshi *et al.*

[31], Spellberg *et al.* [32] and in the Supplementary Information.

Interferometric time-resolved experiments were performed with 1.6 eV (774 nm) photons with controlled time-delay and phase with a Michelson Interferometer (Figure S15). Photons are incident on a 50/50 beam splitter (Thorlabs BSW26R), half one path is directed onto a 0 degree mirror while the other is directed onto a 0 degree mirror mounted to a mechanical delay stage (motorized linear stage, Newport, XMS50-S). The pulses then are recombined with the same beamsplitter and directed onto a series of steering mirrors before being focused into the UHV chamber through a lens and Rhodium mirror mounted in the microscope column.

C. Simulations of HPPs

Both numerical and finite-difference time-domain (FDTD) simulations were used to model the hyperbolic polaritons. Both approaches consider a stack consisting of a MoOCl₂ flake with thickness d on top of 2 nm native SiO₂ on top of 380 μm silicon(100). The dielectric functions of the SiO₂ and silicon were obtained from the SOPRA data bank (<https://www.spectra.com/sopra.html>) and the Handbook of Optical Constants of Solids, respectively [53]. We conducted our simulations using the recently reported dielectric function of MoOCl₂ [15].

A transfer matrix method [54, 55] was used to calculate the dispersion relationships for MoOCl₂. This approach has been successfully employed before to model polaritons observed with scattering near-field optical microscopy [10, 17, 56] as well as PEEM[29, 57]. Details and derivations can be found in reference Rieger *et al.* [29], Raab *et al.* [57].

FDTD simulations were done with Lumerical by Ansys [58] to determine the spatial and temporal field distributions within our sample stack ($d=200\text{nm}$) with nanometer and femtosecond resolution for incident laser wavelength 774 nm. nP-PEEM images were reproduced based on the electric fields from the FDTD output since the PEEM signal can be expressed by $\int (E_x + E_y + E_z)^{2n} dt$ [41, 59, 60]. A field-time monitor was used to record the time evolution of fields to reproduce 4P-PEEM image of Figure 2F. Further details and example of nP-PEEM image simulations with FDTD can be found in Ghosh *et al.* [60]. The dielectric function of silver used for reference simulation implemented in the Lumerical FDTD software are based on fitting of experimental dielectric functions from Johnson and Christy [61].

ASSOCIATED CONTENT

The Supplementary Information includes optical microscopy images of investigated MoOCl₂ flakes, static

PEEM images, polarized Raman spectroscopy, AFM flake thickness characterization, details of data fitting for extraction of dispersion, group velocity, and phase velocities, details of calibration of the laser polarization. Supplementary Movies are included for Flake B (Figure 3) and Flake C (Figure 4) demonstrating space time propagation of HPPs. Another Supplementary Movie shows polarization dependent optical microscopy of Flake B emphasizing the strong optical anisotropy in MoOCl₂.

AUTHOR CONTRIBUTIONS

S.B.K. conceived of the study. A.G. and C. R. performed the experiments with help from J.L.S.. A.G. and C.R. performed the simulations. A.M. provided the samples. A.G., C.R., and J.L.S. performed the data analysis with help and input from S.B.K.. S.B.K., A.G., C.R., and J.L.S. prepared the figures. A.G., C.R. and S.B.K. wrote the manuscript with contributions from all authors. S.B.K. supervised the project and procured funding.

ACKNOWLEDGMENTS

We acknowledge Ryo Mizuta Graphics for providing 3D illustrations as part of this manuscript's figures and Dr. Karen Watters for help with the scientific writing and editing.

This work was funded by the Air Force Office of Scientific Research (FA9550-22-1-0224). This work made use of the shared facilities at the University of Chicago Materials Research Science and Engineering Center, supported by the National Science Foundation under award number DMR-2011854. This work was completed in part with resources provided by the University of Chicago's Research Computing Center. A.G. acknowledges support from a MRSEC-funded Kadanoff-Rice fellowship (DMR-2011854).

- [1] S. Dai, Q. Ma, T. Andersen, A. S. McLeod, Z. Fei, M. K. Liu, M. Wagner, K. Watanabe, T. Taniguchi, M. Thiemens, F. Keilmann, P. Jarillo-Herrero, M. M. Fogler, and D. N. Basov, Subdiffractional focusing and guiding of polaritonic rays in a natural hyperbolic material, *Nat. Commun.* **6**, 6963 (2015).
- [2] J. S. Gomez-Diaz, M. Tymchenko, and A. Alù, Hyperbolic plasmons and topological transitions over uniaxial metasurfaces, *Phys. Rev. Lett.* **114**, 233901 (2015).
- [3] D. J. Roth, A. V. Krasavin, A. Wade, W. Dickson, A. Murphy, S. Kéna-Cohen, R. Pollard, G. A. Wurtz, D. Richards, S. A. Maier, and A. V. Zayats, Spontaneous emission inside a hyperbolic metamaterial waveguide, *ACS Photonics* **4**, 2513 (2017).
- [4] V. M. Agranovich and V. L. Ginzburg, *Spatial Dispersion in Crystal Optics and the Theory of Excitons*, edited by R. E. Marshak, Vol. 18 (Interscience Publishers, New York, 1966).
- [5] V. G. Veselago, The electrodynamics of substances with simultaneously negative values of ϵ and μ , *Soviet Phys.-Uspekhi* **10**, 509 (1968).
- [6] J. Pendry, A. Holden, D. Robbins, and W. Stewart, Magnetism from conductors and enhanced nonlinear phenomena, *IEEE Trans. Microw. Theory* **47**, 2075 (1999).
- [7] J. B. Pendry, Negative refraction makes a perfect lens, *Phys. Rev. Lett.* **85**, 3966 (2000).
- [8] M. N. Gjerding, R. Petersen, T. G. Pedersen, N. A. Mortensen, and K. S. Thygesen, Layered van der Waals crystals with hyperbolic light dispersion, *Nat. Commun.* **8**, 320 (2017).
- [9] J. Sun, N. M. Litchinitser, and J. Zhou, Indefinite by nature: From ultraviolet to terahertz, *ACS Photonics* **1**, 293 (2014).
- [10] S. Dai, Z. Fei, Q. Ma, A. S. Rodin, M. Wagner, A. S. McLeod, M. K. Liu, W. Gannett, W. Regan, K. Watanabe, T. Taniguchi, M. Thiemens, G. Dominguez, A. H. C. Neto, A. Zettl, F. Keilmann, P. Jarillo-Herrero, M. M. Fogler, and D. N. Basov, Tunable phonon polaritons in atomically thin van der Waals crystals of boron nitride, *Science* **343**, 1125 (2014).
- [11] W. Ma, G. Hu, D. Hu, R. Chen, T. Sun, X. Zhang, Q. Dai, Y. Zeng, A. Alù, C.-W. Qiu, and P. Li, Ghost hyperbolic surface polaritons in bulk anisotropic crystals, *Nature* **596**, 362 (2021).
- [12] J. Taboada-Gutiérrez, G. Álvarez Pérez, J. Duan, W. Ma, K. Crowley, I. Prieto, A. Bylinkin, M. Autore, H. Volkova, K. Kimura, T. Kimura, M.-H. Berger, S. Li, Q. Bao, X. P. A. Gao, I. Errea, A. Y. Nikitin, R. Hillenbrand, J. Martín-Sánchez, and P. Alonso-González, Broad spectral tuning of ultra-low-loss polaritons in a van der Waals crystal by intercalation, *Nat. Mater.* **19**, 964 (2020).
- [13] W. Ma, P. Alonso-González, S. Li, A. Y. Nikitin, J. Yuan, J. Martín-Sánchez, J. Taboada-Gutiérrez, I. Amenabar, P. Li, S. Vélez, C. Tollan, Z. Dai, Y. Zhang, S. Sriram, K. Kalantar-Zadeh, S.-T. Lee, R. Hillenbrand, and Q. Bao, In-plane anisotropic and ultra-low-loss polaritons in a natural van der Waals crystal, *Nature* **562**, 557 (2018).
- [14] H. Schäfer and J. Tillack, MoOCl_2 darstellung, chemischer transport, eigenschaften, *J. Less-Common Metals* **6**, 152 (1964).
- [15] J. Zhao, W. Wu, J. Zhu, Y. Lu, B. Xiang, and S. A. Yang, Highly anisotropic two-dimensional metal in monolayer MoOCl_2 , *Phys. Rev. B* **102**, 245419 (2020).
- [16] H. Gao, C. Ding, L. Sun, X. Ma, and M. Zhao, Robust broadband directional plasmons in a MoOCl_2 monolayer, *Phys. Rev. B* **104**, 205424 (2021).
- [17] F. L. Ruta, Y. Shao, S. Acharya, A. Mu, N. H. Jo, S. H. Ryu, D. Balatsky, Y. Su, D. Pashov, B. S. Y. Kim, M. I. Katsnelson, J. G. Analytis, E. Rotenberg, A. J. Millis, M. v. Schilfgaarde, and D. N. Basov, Good plasmons in a bad metal, *Science* **387**, 786 (2025).
- [18] G. Venturi, A. Mancini, N. Melchioni, S. Chiodini, and A. Ambrosio, Visible-frequency hyperbolic plasmon polaritons in a natural van der Waals crystal, *Nat. Commun.* **15**, 9727 (2024).
- [19] Y. Zhang, L.-F. Lin, A. Moreo, and E. Dagotto, Orbital-selective Peierls phase in the metallic dimerized chain MoOCl_2 , *Phys. Rev. B* **104**, L060102 (2021).
- [20] Z. Wang, M. Huang, J. Zhao, C. Chen, H. Huang, X. Wang, P. Liu, J. Wang, J. Xiang, C. Feng, Z. Zhang, X. Cui, Y. Lu, S. A. Yang, and B. Xiang, Fermi liquid behavior and colossal magnetoresistance in layered MoOCl_2 , *Phys. Rev. Materials* **4**, 041001 (2020).
- [21] M. Dąbrowski, Y. Dai, and H. Petek, Ultrafast photoemission electron microscopy: Imaging plasmons in space and time, *Chem. Rev.* **120**, 6247 (2020).
- [22] M. Dąbrowski, Y. Dai, A. Argondizzo, Q. Zou, X. Cui, and H. Petek, Multiphoton photoemission microscopy of high-order plasmonic resonances at the Ag/vacuum and Ag/Si interfaces of epitaxial silver nanowires, *ACS Photonics* **3**, 1704 (2016).
- [23] A. Kubo, N. Pontius, and H. Petek, Femtosecond microscopy of surface plasmon polariton wave packet evolution at the silver/vacuum interface, *Nano Lett.* **7**, 470 (2007).
- [24] Y. Dai, Z. Zhou, A. Ghosh, R. S. K. Mong, A. Kubo, C.-B. Huang, and H. Petek, Plasmonic topological quasiparticle on the nanometre and femtosecond scales, *Nature* **588**, 616 (2020).
- [25] D. N. Basov, M. M. Fogler, and F. J. García de Abajo, Polaritons in van der Waals materials, *Science* **354**, aag1992 (2016).
- [26] M. Aeschlimann, M. Bauer, D. Bayer, T. Brixner, F. J. García de Abajo, W. Pfeiffer, M. Rohmer, C. Spindler, and F. Steeb, Adaptive subwavelength control of nano-optical fields, *Nature* **446**, 301 304 (2007).
- [27] M. Bauer, C. Wiemann, J. Lange, D. Bayer, M. Rohmer, and M. Aeschlimann, Phase propagation of localized surface plasmons probed by time-resolved photoemission electron microscopy, *Appl. Phys. A* **88**, 473 (2007).
- [28] Y. Gong, A. G. Joly, D. Hu, P. Z. El-Khoury, and W. P. Hess, Ultrafast imaging of surface plasmons propagating on a gold surface, *Nano Lett.* **15**, 3472 (2015).
- [29] J. Rieger, A. Ghosh, J. L. Spellberg, C. Raab, A. Mohan, P. P. Joshi, and S. B. King, Imaging and simulation of surface plasmon polaritons on layered 2D MXenes, *Sci. Adv.* **11**, eads3689 (2025).
- [30] T. Eul, M. Sabir, V. DeManuel-Gonzalez, F. Diekmann, K. Rossnagel, and M. Bauer, Photoemission electron microscopy of exciton-polaritons in thin WSe_2 waveguides, *ACS Photonics* **10.1021/acsp Photonics.5c00290** (2025).
- [31] P. P. Joshi, R. Li, J. L. Spellberg, L. Liang, and S. B. King, Nanoimaging of the edge-dependent optical polarization anisotropy of black phosphorus, *Nano Lett.* **22**, 3180 (2022).

- [32] J. L. Spellberg, L. Kodaimati, P. P. Joshi, N. Mirzajani, L. Liang, and S. B. King, Electronic structure orientation as a map of in-plane antiferroelectricity in β' - In_2Se_3 , *Sci. Adv.* **10**, eado2136 (2024).
- [33] A. Ghosh, J. L. Spellberg, and S. B. King, Polarization-dependent photoemission electron microscopy for domain imaging of inorganic and molecular materials, *J. Chem. Phys.* **161**, 110901 (2024).
- [34] P. Kahl, S. Wall, C. Witt, C. Schneider, D. Bayer, A. Fischer, P. Melchior, M. H.-v. Hoegen, M. Aeschlimann, and F.-J. M. z. Heringdorf, Normal-incidence photoemission electron microscopy (NI-PEEM) for imaging surface plasmon polaritons, *Plasmonics* **9**, 1401 (2014).
- [35] P. Shekhar, M. Malac, V. Gaiand, N. Dalili, A. Meldrum, and Z. Jacob, Momentum-resolved electron energy loss spectroscopy for mapping the photonic density of states, *ACS Photonics* **4**, 1009 (2017).
- [36] P. Shekhar, S. Pendharker, D. Vick, M. Malac, and Z. Jacob, Fast electrons interacting with a natural hyperbolic medium: bismuth telluride, *Opt. Express* **27**, 6970 (2019).
- [37] A. W. Rossi, M. R. Bourgeois, C. Walton, and D. J. Masiello, Probing the polarization of low-energy excitations in 2D materials from atomic crystals to nanophotonic arrays using momentum-resolved electron energy loss spectroscopy, *Nano Lett.* **24**, 7748 (2024).
- [38] E. E. Narimanov, Dyakonov waves in biaxial anisotropic crystals, *Phys. Rev. A* **98**, 013818 (2018).
- [39] M. P. Seah and W. A. Dench, Quantitative electron spectroscopy of surfaces: A standard data base for electron inelastic mean free paths in solids, *Surf. Interface Anal.* **1**, 2 (1979).
- [40] G. Spektor, D. Kilbane, A. K. Mahro, M. Hartelt, E. Prinz, M. Aeschlimann, and M. Orenstein, Mixing the light spin with plasmon orbit by nonlinear light-matter interaction in gold, *Phys. Rev. X* **9**, 021031 (2019).
- [41] D. Podbiel, P. Kahl, A. Makris, B. Frank, S. Sindermann, T. J. Davis, H. Giessen, M. H.-v. Hoegen, and F.-J. M. z. Heringdorf, Imaging the nonlinear plasmoemission dynamics of electrons from strong plasmonic fields, *Nano Lett.* **17**, 6569 (2017).
- [42] A. A. High, R. C. Devlin, A. Dibos, M. Polking, D. S. Wild, J. Perczel, N. P. de Leon, M. D. Lukin, and H. Park, Visible-frequency hyperbolic metasurface, *Nature* **522**, 192 (2015).
- [43] F. Goos and H. Hänchen, Ein neuer und fundamentaler versuch zur totalreflexion, *Ann. Phys.* **436**, 333 (1947).
- [44] P. Melentiev, A. Kuzin, D. Negrov, and V. Balykin, SPP waveguide based on the goos-hänchen effect, *Opt. Lett.* **46**, 4029 (2021).
- [45] J.-H. Kang, S. Wang, Z. Shi, W. Zhao, E. Yablonovitch, and F. Wang, Goos-hänchen shift and even-odd peak oscillations in edge-reflections of surface polaritons in atomically thin crystals, *Nano Lett.* **17**, 1768 (2017).
- [46] V. J. Yallapragada, A. P. Ravishankar, G. L. Mulay, G. S. Agarwal, and V. G. Achanta, Observation of giant goos-hänchen and angular shifts at designed metasurfaces, *Sci. Rep.* **6**, 19319 (2016).
- [47] K. Liu, S. Sun, A. Majumdar, and V. J. Sorger, Fundamental scaling laws in nanophotonics, *Sci. Rep.* **6**, 37419 (2016).
- [48] D. Lee, S. So, G. Hu, M. Kim, T. Badloe, H. Cho, J. Kim, H. Kim, C.-W. Qiu, and J. Rho, Hyperbolic metamaterials: fusing artificial structures to natural 2D materials, *eLight* **2**, 1 (2022).
- [49] Z. Chen, S. Xia, S. Yang, B. Wang, S. Tang, Y. Yang, T. Cui, S. Liu, and H. Wang, Ferroelectric control of diverse hyperbolic polaritons in the visible spectrum, *npj Computational Materials* **11**, 134 (2025).
- [50] A. Grankin and V. Galitski, Interplay of hyperbolic plasmons and superconductivity, *Phys. Rev. B* **108**, 094506 (2023).
- [51] A. Aigner, J. M. Dawes, S. A. Maier, and H. Ren, Nanophotonics shines light on hyperbolic metamaterials, *Light: Science & Applications* **11**, 9 (2022).
- [52] J. S. Gomez-Diaz, M. Tymchenko, and A. Alù, Hyperbolic metasurfaces: surface plasmons, light-matter interactions, and physical implementation using graphene strips, *Opt. Mater. Express* **5**, 2313 (2015).
- [53] A. Borghesi, G. Guizzetti, and E. Palik, *Handbook of Optical Constants of Solids* (Elsevier, 1991).
- [54] N. C. Passler and A. Paarmann, Generalized 4×4 matrix formalism for light propagation in anisotropic stratified media: study of surface phonon polaritons in polar dielectric heterostructures, *J. Opt. Soc. Am. B* **34**, 2128 (2017).
- [55] N. C. Passler, X. Ni, G. Carini, D. N. Chigrin, A. Alù, and A. Paarmann, Layer-resolved resonance intensity of evanescent polariton modes in anisotropic multilayers, *Phys. Rev. B* **107**, 235426 (2023).
- [56] F. Mooshammer, S. Chae, S. Zhang, Y. Shao, S. Qiu, A. Rajendran, A. J. Sternbach, D. J. Rizzo, X. Zhu, P. J. Schuck, J. C. Hone, and D. N. Basov, In-plane anisotropy in biaxial ReS_2 crystals probed by nano-optical imaging of waveguide modes, *ACS Photonics* **9**, 443 (2022).
- [57] C. Raab, J. Rieger, A. Ghosh, J. L. Spellberg, and S. B. King, Surface plasmons in two-dimensional MXenes, *J. Phys. Chem. Lett.* , 11643 (2024).
- [58] A. Taflove, S. C. Hagness, and M. Picket-May, Computational electromagnetics: the finite-difference time-domain method, *The Electrical Engineering Handbook* **3**, 629 (2005).
- [59] Y. Dai, M. Dąbrowski, V. A. Apkarian, and H. Petek, Ultrafast microscopy of spin-momentum-locked surface plasmon polaritons, *ACS Nano* **12**, 6588 (2018).
- [60] A. Ghosh, S. Yang, Y. Dai, Z. Zhou, T. Wang, C.-B. Huang, and H. Petek, A topological lattice of plasmonic merons, *App. Phys. Rev.* **8**, 10.1063/5.0062133 (2021).
- [61] P. B. Johnson and R. W. Christy, Optical constants of the noble metals, *Phys. Rev. B* **6**, 4370 (1972).